

## On the Appearance of Translucent Edges

Ioannis Gkioulekas  
Harvard SEAS

igkiou@seas.harvard.edu

Bruce Walter  
Cornell University

bruce.walter@cornell.edu

Edward H. Adelson  
Massachusetts Institute of Technology

adelson@csail.mit.edu

Kavita Bala  
Cornell University

kb@cs.cornell.edu

Todd Zickler  
Harvard SEAS

zickler@seas.harvard.edu

### Abstract

*Edges in images of translucent objects are very different from edges in images of opaque objects. The physical causes for these differences are hard to characterize analytically and are not well understood. This paper considers one class of translucency edges—those caused by a discontinuity in surface orientation—and describes the physical causes of their appearance. We simulate thousands of translucency edge profiles using many different scattering material parameters, and we explain the resulting variety of edge patterns by qualitatively analyzing light transport. We also discuss the existence of shape and material metamers, or combinations of distinct shape or material parameters that generate the same edge profile. This knowledge is relevant to visual inference tasks that involve translucent objects, such as shape or material estimation.*

### 1. Introduction

Translucency is a common visual phenomenon. It occurs whenever light penetrates a material and scatters within it before re-emerging toward the observer. This internal scattering can create a variety of image effects, depending on an object's shape and material; its distance from the observer; and the composition of the lighting around it. Common human experience suggests that these image effects contain useful material information, and there is psychophysical evidence that humans can discriminate subtle differences in translucent appearance, recognize translucent material categories, and make inferences about physical scattering parameters [2, 11, 13, 27].

There ought to be specific patterns of image brightness, or their statistics, that constrain the set of plausible shapes and materials in an image of translucency. If we understood these patterns, we could use them to develop inference algorithms, analogous to those that exist for opaque scenes.

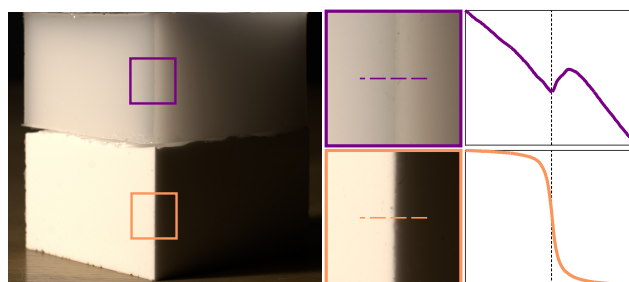


Figure 1: Radiance profiles at a discontinuity in orientation. The *wedge configuration* is a horizontal cross-section of two planar faces that meet in a vertical line. Here it is lit from the left. If the material were opaque (as below) the profile would be a step edge. When it is translucent (as above), the profiles can be very different, often with multiple extrema that are displaced from the discontinuity.

One prominent class of brightness patterns is edges, or sharp local changes in image brightness. Edges have a variety of causes—cast shadows, material boundaries, occlusions, *etc.*—and models of edges play prominent roles in a variety of inference algorithms, including contour detection, deblurring, and material recognition. In this paper, we focus on edges that are caused by a discontinuous change in surface orientation, such as at the corners of the cubes in Figure 1. Locally, this geometry can be modeled by the one-dimensional *wedge* of Figure 2. We use this as an archetypal configuration for studying edges of translucency.

The radiance profile observed from an opaque wedge would be the familiar step function, which is a popular edge model in image processing and computer vision. But the radiance profiles for translucent wedges are very different. As shown in Figure 1, they tend to exhibit multiple extrema in the vicinity of an orientation discontinuity, and these extrema are often displaced away from the geometric discontinuity.

The physical causes of these profile phenomena are not well understood. One reason is that they are hard to describe

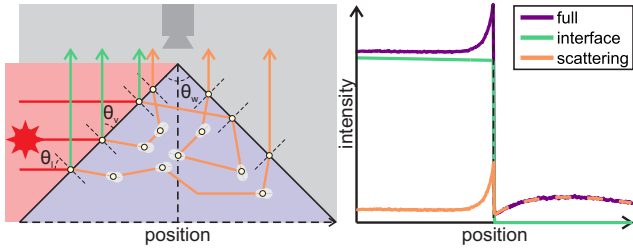


Figure 2: *Left*: Wedge model. A homogeneous translucent volume forms a perfect corner with internal angle  $\theta_w$ , and this corner is lit from the side (direction  $\theta_l$ ) and viewed from above (direction  $\theta_v$ ). *Right*: A typical radiance profile measured by the camera. It is the sum of an interface component and an internal scattering component. We consider only the scattering component in the rest of this paper.

analytically. For the translucent wedge configuration, radiance profiles represent the combination of interface reflection with various orders of volume scattering events. They result from interactions between view and light directions, refractive index, optical density, scattering albedo, and scattering phase function. There is unlikely to be an analytic solution to the radiative transport equation for this scenario, and we have yet to find a useful approximate solution.

Our strategy is to explore these phenomena empirically through simulation. Using Monte Carlo rendering techniques, we generate a database of thousands of radiance profiles for many scattering materials and wedge configurations. We catalog the variety of profiles we observe, and we qualitatively explain their features by analyzing light transport in terms of interface events, single-scattering, mid-order scattering, and high-order scattering (diffusion). We also discuss the existence of shape and material metamers—combinations of distinct shape or material parameters that nonetheless generate the same radiance profile.

Together, our analyses provide a comprehensive description of the physical causes of the radiance profiles that are induced by surface orientation discontinuities, or geometric edges, on translucent materials. This is a foundation for understanding how these profiles can be used for visual inference tasks, where we want to estimate shape and material information from images that include translucency.

## 2. Scattering near an orientation discontinuity

We consider a wedge with a perfectly sharp corner, made of a single, homogeneous translucent material. A two-dimensional cross-section of this scene is shown in Figure 2. The wedge is illuminated from the side by collimated light, and is imaged from above by an orthographic camera. This geometry has three degrees of freedom: the illumination and view directions  $\theta_l$ ,  $\theta_v$ , and the wedge angle  $\theta_w$ .

The radiance profile measured by the camera is the sum of two components, as shown in Figure 2. The first is an interface component, which corresponds to light that is reflected at the wedge surface, without entering the material volume. We assume the interface is smooth, so this component is determined by the index of refraction  $\eta$  and the light and view angles  $\theta_l$ ,  $\theta_v$ , as described by the Fresnel equations. The interface component has the familiar shape of a step function, with the step occurring exactly at the image-projection of the orientation discontinuity. Since it does not depend on scattering, does not create an interesting variety of radiance profiles, and has been well-studied elsewhere, we ignore this component for the remainder of the paper. However, one should keep in mind that this step-shaped interface component will dominate whenever the view and illumination directions are close to being mirrored.

The second component of the radiance profile corresponds to light that is refracted at the interface and travels inside the volume. There, it experiences scattering and internal reflection, perhaps many times, before traversing the interface again toward the camera. We call this the scattering component. The refraction and internal reflection at the material-air interfaces are modeled by the Fresnel equations and involve a single material parameter, the index of refraction  $\eta$ . Scattering occurs as light propagates through the material medium and interacts with material structures. This results in multiple volume events that each cause absorption or change of propagation direction.

Scattering is governed by three material parameters that appear in the radiative transfer equation [6, 16]: the density (extinction coefficient)  $\sigma_t$ ; the scattering albedo  $\alpha$ ; and the scattering phase function  $p(\theta)$ ,  $\theta \in [0, \pi)$ . Density  $\sigma_t$  controls the spatial frequency of volume events. Albedo  $\alpha \leq 1$  is a probability controlling whether light at a volume event is scattered ( $\text{Pr} = \alpha$ ) or absorbed ( $\text{Pr} = 1 - \alpha$ ). Finally, phase function  $p$  is a probability distribution function on the sphere of directions that describes the angular distribution of light scattered at volume events. As is usual, we assume the phase function is cylindrically-symmetric and invariant to rotations of the incident direction, so it only depends on angle  $\theta$  relative to the incident direction.

To study the appearance of the scattering component of the radiance profiles, we use Monte Carlo rendering for the full (three-dimensional) wedge scene to generate radiance profiles for different combinations of geometry and material parameters. For geometry, we consider illumination and view directions ranging from grazing to almost normal incidence, excluding larger angles to prevent illumination of the right surface and ensure that both surfaces are visible:  $\theta_v, \theta_l \in \{15^\circ, 30^\circ, 45^\circ, 60^\circ, 75^\circ\}$ , and  $\theta_w \in \{30^\circ, 60^\circ, 90^\circ\}$ . For materials, we focus on non-emissive, low-absorption dielectrics, which include a

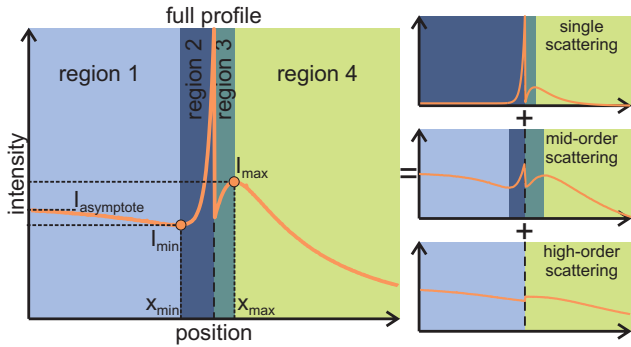


Figure 3: Left: Representative edge radiance profile for a translucent material. A profile is typically made up of four qualitatively distinct regions, highlighted with different background colors. These give rise to characteristic features, in the form of local radiance extrema away from the geometric edge, as shown. Right: Decomposition of the profile into single, mid-order, and high-order scattering components. Different subsets of the four qualitative regions of the full profile appear in the three scattering components, indicated by matching colors.

wide range of common translucent materials such as soap and wax, and exclude near-transparent absorptive liquids. Specifically, we use:  $\eta \in \{1.3, 1.4, 1.5, 1.6, 1.7, 1.8\}$ ,  $\alpha \in \{0.9, 0.92, 0.94, 0.96, 0.98, 1\}$ , and a phase function dictionary consisting of linear combinations of Henyey-Greenstein and von Mises-Fisher lobes [13]. We use density  $\sigma_t = 1 \text{ mm}^{-1}$  and a field of view (length of “position” axis) of approximately one inch. We note that these values are arbitrary, due to a scale ambiguity between density and field of view: doubling the density and halving the (linear) field of view has no effect on the radiance profile. The database is available at the project page [1], and we use it, along with the corresponding parameter ranges, throughout the rest of the paper. Section 4 discusses additional renderings for wedge scenes with various non-idealities. Finally, we have produced additional renderings using Lorentz-Mie [12] and measured [14] phase functions, to validate that our findings are not biased by our dictionary selection.

### 3. Behavior of Radiance Profiles

A typical translucent edge profile, as shown in Figure 3, has four basic regions. These are highlighted in the figure using different background colors. Starting from the left (illuminated side) in region 1, radiance decreases from a steady value to a local minimum at some location  $x_{\min}$ . Then it increases sharply in region 2, before making a discontinuous jump at the projection of the wedge’s apex. It rises again in region 3, eventually reaching a local maximum at some  $x_{\max}$ . In region 4, it decreases monotonically to zero. These qualitative features are *characteristic* of translucency

because they are distinct from the sigmoidal edge profiles of opaque materials. As we will describe later, the local extrema that are displaced from the geometric discontinuity are particularly characteristic, since they appear even when the geometry deviates from the ideal wedge shape (Figure 7). These features could be used to distinguish translucent materials from opaque ones.

To understand the physical processes that produce these characteristic features, it is helpful to separately examine two limit scattering components: light that has only scattered once (single scattering) and light that has scattered many times (high-order scattering).

#### 3.1. Single Scattering

The radiance profile from just the single-scattering component of the light transport is shown in Figure 3. Its expression can be easily derived analytically, though it is more intuitive to describe it qualitatively in two steps. First, we describe the zero-scattering lightfield inside the material volume. Then, we trace view rays through this lightfield to produce a radiance profile. We use Figure 4 for reference.

Consider a light ray  $l$  (shown in red) entering from the left side of the wedge. It first gets refracted at point  $q_1$  of the air-material interface. Then, the ray propagates straight inside the medium, while also being attenuated due to absorption and outscatter. After the ray reaches the right edge, at point  $q_2$ , it gets reflected internally, either partially or totally, depending on whether the angle of incidence is larger than the critical angle for the volume’s index of refraction. The ray then propagates in the reflected direction.

This process produces a total zero-scattering lightfield that is the sum of two components. The first is light that has not undergone internal reflection (the light ray  $l$  between points  $q_1$  and  $q_2$ ). It extends everywhere inside the wedge volume, and at any point radiance is non-zero along a single direction. The second component corresponds to light that is internally reflected (the light ray  $l$  after point  $q_2$ ), and extends spatially only in the part of the wedge volume that is reached by reflected rays. This area is bounded from the left by a line parallel to the reflected rays and starting at the apex of the wedge, as shown in Figure 4. We refer to this line as the *internal reflection boundary*, and we visualize it as a dotted black line inside the wedge. The reflected lightfield component is also non-zero along a single direction. The superposition of these two components results in a total zero-scattering lightfield that has two distinct regions, with the region right of the internal reflection boundary having a higher total flux (the sum of radiance in all directions) than the region left of it, as shown in Figure 4.

To relate the zero-scattering lightfield to the single-scattering radiance profile, we trace *view rays* that start from

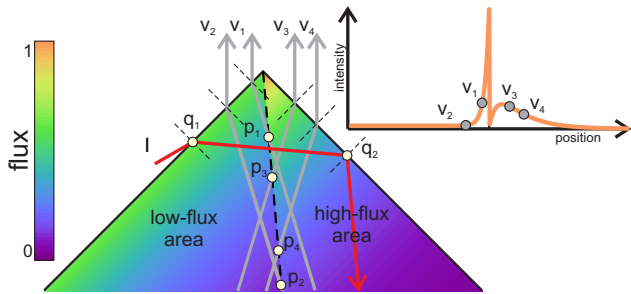


Figure 4: Flux field (left) and radiance profile (right) produced by single scattering. Grey lines are back-projected view rays that correspond to different locations on the image plane. There is a discontinuity along a line in the flux field (dotted black line), and this separates the volume into two distinct areas. The boundary between the areas is parallel to, and created by, internally reflected light rays (red).

the camera, enter the wedge, and integrate radiance as they travel inside the material. We show view rays in Figure 4 in gray. We consider first a view ray  $v_1$  entering from a position to the left of the edge. After refraction, the ray originally travels through (and integrates radiance from) the low-flux area of the zero-scattering lightfield, left of the internal reflection boundary. The ray eventually intersects the reflection boundary, at point  $p_1$ , and begins to integrate radiance from the high-flux area of the lightfield. A view ray  $v_2$  that is farther to the left from the edge travels a larger distance inside the low-flux area and crosses the reflection boundary at a point  $p_2$  deeper inside the medium. Because of attenuation, this means that  $v_2$  integrates exponentially less radiance from the high-flux area than ray  $v_1$ . As a result, the radiance profile at the point corresponding to  $v_1$  has a higher value than at the point for  $v_2$ . More generally, the single-scattering radiance profile left of the geometric edge decreases exponentially, until it asymptotes to a value measured by view rays that receive negligible contributions from the high-flux area of the lightfield.

The behavior to the right of the edge is different. A view ray  $v_3$  entering this side of the wedge penetrates the high-flux area, crosses the internal reflection boundary at point  $p_3$ , and continues in the low-flux area. A view ray  $v_4$  farther to the right travels longer inside the high-flux area, up until point  $p_4$ . Even though the high-flux part of its path is longer, ray  $v_4$  integrates less radiance. This is because the part of the high-flux area that it travels has experienced greater attenuation. This illustrates a tradeoff as we move rightward. View rays span increasingly more of the high-flux area, but the flux in that area weakens from attenuation. The larger distances dominate near the edge, and the radiance profile rises. Eventually, attenuation takes over, and the profile starts to decrease. The result is a characteristic local maximum in the radiance profile right of the edge,

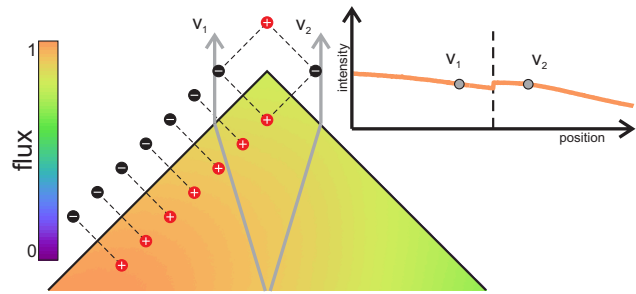


Figure 5: Flux field (left) and radiance profile (right) produced by high-order-scattering light transport in the wedge geometry. The flux field can be approximated by one produced by “positive” sources inside the wedge and “negative” sources outside. The presence of more negative sources near the edge results in lower flux in that area.

as shown in Figure 4. The exact position and value of this local maximum depends on the material parameters.

### 3.2. High-Order Scattering

The multipole approximation [18, 9] provides a good mental model for understanding the lightfield produced by high-order scattering. This approximation replaces the collimated incident light with virtual positive and negative sources along the wedge boundary, inside and outside of the wedge respectively. The sources are placed so that they satisfy the boundary conditions of the diffusion equation [16], which approximately describes high-order scattering. For the wedge geometry, this is shown in Figure 5, where we see that the additional boundary at the edge requires the placement of negative sources on the right side of the wedge. These extra negative sources result in less radiance near the corner than at other points along the illuminated wedge side boundary. In turn, by tracing view rays  $v_1$  starting left of the edge, we see that the reduced radiance near the wedge corner produces a monotonically decreasing radiance profile left of the geometric edge. For the part of the profile right of the geometric edge, a view ray  $v_2$  travels through parts of the lightfield that are progressively more attenuated the farther the ray is from the edge, resulting again in a monotonically decreasing radiance profile.

### 3.3. Mid-Order Scattering

The shapes of radiance profiles also depends on mid-order scattering. For intuition, it can be compared to single scattering. As described above, internal reflection produces a sharp discontinuity in the zero-scattering lightfield inside the wedge volume, the internal reflection boundary. The exact position of this discontinuity relative to view rays strongly affects the shape of the single-scattering radiance profile. In particular, as we explained earlier through Figure 4, if view rays left of the edge intersect with the re-

flection boundary, the radiance profile has an exponential rise immediately left of the edge. It is possible, however, to select an illumination direction such that left view rays never intersect with the reflection boundary, as shown in the left column of Figure 6. In this case, left view rays never enter the high-flux area of the zero-scattering lightfield, and the single-scattering radiance profile is constant everywhere left of the edge.

Mid-order scattering has the effect of *blurring* the discontinuity at the internal reflection boundary, as radiance gets scattered from the high-flux towards the low-flux area of the lightfield. This is shown at the bottom row of Figure 6, which plots 1D cross-sections through the single and mid-order scattering flux fields. The sharp discontinuity at the reflection boundary  $p$  seen in the single-scattering field is blurred into a smooth transition in the mid-order field. Due to this blurring, left view rays near the boundary can pick up some radiance from the high-flux area even if they do not intersect the boundary. Therefore, there can be an exponential rise region left of the edge in the mid-order-scattering radiance profile (and in the full radiance profile), even when it is not present in the single-scattering radiance profile (left column of Figure 6).

#### 4. Effects of Non-Idealities

The analysis of the previous section is based on an ideal wedge model. Though convenient for analysis, such exact geometry is unlikely to be encountered in real-world scenes. It is therefore worth understanding how the characteristic features of translucent profiles are affected by deviations from this model.

There are typically three non-idealities that one will encounter in a realization of the wedge geometry: First, it is impossible to have perfectly collimated light and an exactly orthographic camera. Second, the surfaces of a real wedge will not be perfectly smooth, but have microstructure resulting in a BRDF that is not perfectly specular. Third, a real wedge will not have an exact corner, but instead will have a bevel of some non-zero radius. In the supplementary material, we use Monte Carlo simulations to examine the effect of each of these non-idealities on edge radiance profiles. The simulations show that non-zero solid angles for the illumination and camera have negligible effect on the shape of the radiance profile. Additionally, radiance profiles maintain all of their characteristic features for a reasonable range of surface roughness values, though unsurprisingly not for very rough interfaces such as etched surfaces. The largest effect comes from having a bevelled, or rounded, wedge apex. It effectively “erases” the profile features whose distance from the apex is less than the radius of the bevel. The exponential rise in region 2 of Figure 3 is particularly susceptible, and it disappears even for small bevels. In contrast,

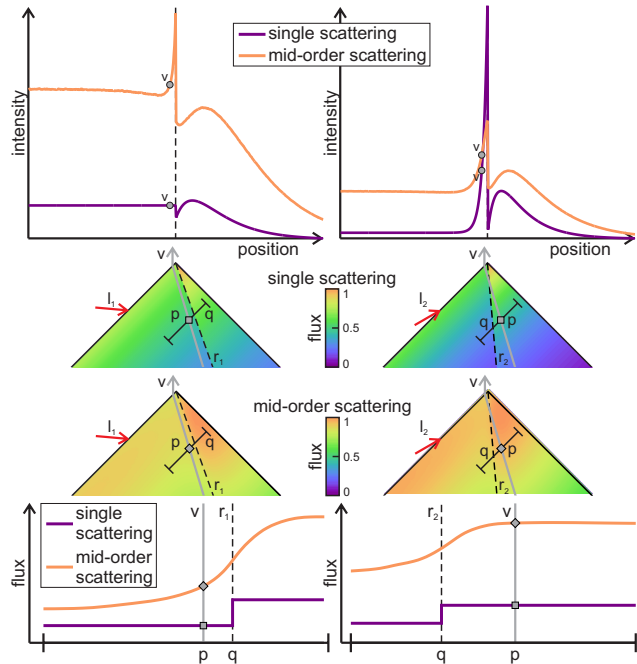


Figure 6: Comparison of single and mid-order scattering for two configurations (left and right column) differing only in illumination direction. The top row shows the radiance profiles for single and mid-order scattering in each case. The middle rows show the corresponding flux fields. The change in illumination direction from  $l_1$  (left) to  $l_2$  (right) also changes the internal reflection boundary (dashed line). A view ray  $v$  entering the wedge left of the geometric edge will not intersect the reflection boundary in the case of  $l_1$ , but will intersect it in the case of  $l_2$ . The bottom graphs show the flux values along the 1D cross-section segment indicated inside the volume. Point  $p$  is intersection of the segment with view ray  $v$ ; point  $q$  is intersection of the segment with the internal reflection boundary.

our simulations show that the local extrema at  $x_{\min}$  and  $x_{\max}$  are quite robust to all non-idealities, including beveling.

In addition to simulations, we captured photographs of translucent wedges under increasingly non-ideal conditions. The top row of Figure 7 shows photographs of wedges we created by mixing clear silicone with different optical scatterers and casting the mixtures into optically smooth molds. These objects have very smooth surfaces and very sharp geometric edges. We photographed these objects using cross-polarization to approximately remove the strong, near specular, interface component [23, 7]. Under these near-ideal conditions, the photographs exhibit all of the characteristic features, including the local minimum and sharp rise left of the geometric edge, and the local maximum right of it. We note that, due to the simultaneously small physical size of the molds and small density of the two materials, regions 1

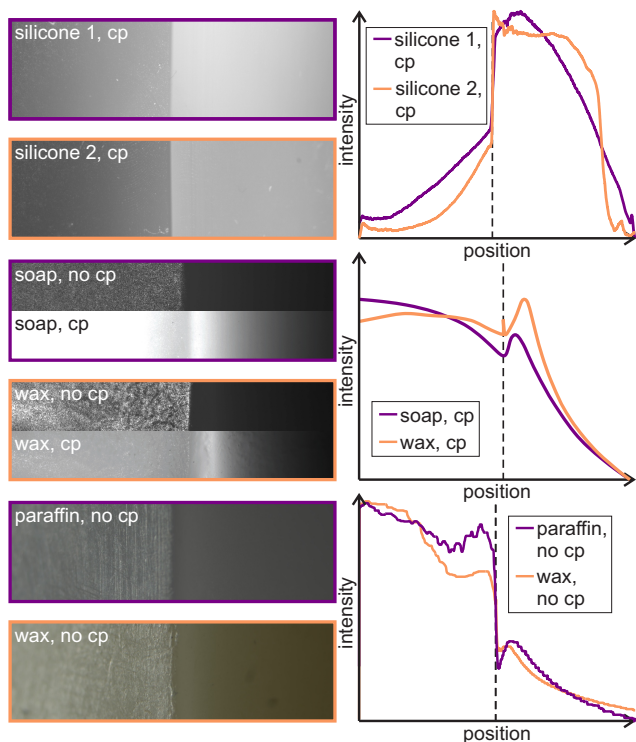


Figure 7: Edges from real-world translucent wedges, photographed with (“cp”) or without (“no cp”) the use of cross-polarization to remove surface reflection. Each row shows cropped wedge photographs (left) and corresponding edge profiles produced by taking horizontal cross-sections of the photographs (right). Top: Wedges with very smooth surfaces and sharp corners. Middle: Wedges with relatively smooth surfaces and moderately beveled corners. Bottom: Wedges with very rough surfaces and very beveled corners.

and 4 of Figure 3 are beyond the field of view.

The middle row of Figure 7 shows photographs captured from objects we created by casting milk soap and paraffin wax into cube molds. The objects have moderate bevel sizes (radii of 2–3mm), and surface roughness comparable to commercial soap bars and wax candles. The photographs are of one corner of each cube under side illumination, with and without cross-polarization (shown top and bottom, respectively). The cross-polarized photographs and graphs show a dramatic shift in the location of the intensity extremum ( $x_{\max}$ ) away from the geometric edge. This creates a striking visual effect when comparing images captured with and without cross-polarization: Without cross-polarization, we can easily detect the geometric edge from the discontinuity in the interface component. Once the interface component is removed, it becomes almost impossible to visually locate the geometric edge.

In the above two cases, the surface is quite smooth, so the interface component is very strong and must be removed

with cross-polarization to make the scattering component more visible. When the surface is less smooth, the interface component is weaker, and the characteristic features of translucency can be observed without cross-polarization. One example is shown in the photographs at the bottom of Figure 7, which were captured without cross-polarization. The photographs are from the corners of cube objects made from different paraffin waxes. The objects have very rough surfaces (evident by the surface artifacts in the photographs) and large bevels. Another example is shown in the top row of Figure 1, which is a photograph of a silicone cube captured without cross-polarization by a very wide (20mm) lens and under very wide illumination. Even with these severe non-idealities, the photographs show a “glow” right of the geometric edge, which is also visible in the respective plotted profiles, and which corresponds to the local maximum  $x_{\max}$  in Figure 3. Conversely, the photograph and profile at the bottom row of Figure 1, corresponding to an almost opaque material, do not show any of the characteristic features of translucent edges.

## 5. Metamerism

The two previous sections demonstrated that the edge radiance profiles of translucent materials are distinctly different from those of opaque materials, with a rich set of features, such as local extrema, that are robust to non-idealities of real-world objects. This appearance and the exact form of the features is the result of a combination of the physical processes of refraction, reflection, and scattering. We can expect a single radiance profile to carry rich information about all the parameters of the underlying object material that control these processes. It is natural, then, to investigate the question of metamerism: Given a radiance profile, are there distinct sets of material and geometry parameters that generate the same radiance profile? Or does the radiance profile uniquely determine the material or shape?

To answer these questions, we used the database of rendered profiles described in Section 2. For each of these profiles, we compute the positions of  $x_{\min}$  and  $x_{\max}$  of the local radiance extrema (see Figure 3); as well as their radiance values normalized in an exposure-independent way,  $I_{\min}/I_{\text{asymptote}}$  and  $I_{\max}/I_{\text{asymptote}}$ . We selected these features as, based on the discussion of the previous section, they can be computed from properly exposed photographs of real translucent objects. We then use changes in these features to examine how each material and geometry parameter affects the appearance of radiance profiles. As with the extrema radiance values, all of the profiles in this section are shown normalized by  $I_{\text{asymptote}}$ , to account for exposure settings. For the profiles, we will also be referring to the four qualitative regions described in Section 3 and shown in Figure 3.

Before feature extraction, as a preprocessing step, we com-

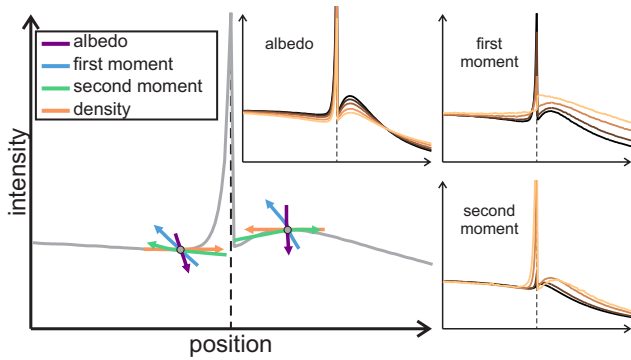


Figure 8: Effect of scattering material parameters on the local extrema features of edge radiance profiles, as defined in Figure 3. The insets show representative sets of profiles where only the indicated parameter changes, with all other material and geometry parameters fixed.

pute analytic fits to the rendered radiance profiles. The fits help reduce noise, and allow us to accurately estimate the features described previously. For the fitting, we use fourth-degree polynomial terms and their exponentiations to produce least-squares fits to the four regions of each radiance profile, as defined in Figure 3. We describe the fitting algorithm in detail in the supplementary material.

### 5.1. Scattering Material Parameters

We first consider the three material parameters controlling volume scattering, defined in Section 2. We use Figure 8 as reference. The figure shows how the local radiance extrema move for increases of the corresponding material parameter.

The effect of density  $\sigma_t$  is straightforward, due to ambiguity with field of view: increasing density from  $\sigma_t$  to  $\sigma'_t$  is equivalent to scaling the position axis by  $\sigma_t/\sigma'_t$ , moving the extrema closer to the geometric edge. A very large density has the effect of collapsing regions 2 and 3 of the profile, and the material and its edges appear essentially opaque.

Increasing the albedo  $\alpha$  results in a decrease of both the normalized intensity of both local extrema, with relatively little effect to their locations. Intuitively, increasing the albedo means reducing absorption, making high-order scattering contribute more strongly relative to low-order scattering. As a result, the local extrema, which are primarily caused by low-order scattering (Section 3), become less prominent.

As the space of phase functions  $p(\theta)$  is infinite dimensional, we focus only on its first two angular moments  $m_1$  and  $m_2$ , which have been shown to dominate translucent appearance [13, 27]. As shown in Figure 8, increasing the first moment (average direction) increases the normalized radiance of the local extrema, with a smaller effect on their locations. At the same time, the radiance contrast in region

2 of the profiles significantly decreases, overall making the local minimum at  $x_{\min}$  less prominent.

The second moment (angular variance) very strongly affects the positions  $x_{\min}$  and  $x_{\max}$  of the local extrema, as well as the contrast of the local maximum at  $x_{\max}$ . Increases in the second moment move the extrema away from the geometric edge, making them very pronounced. Conversely, decreasing the second moment moves the extrema on the edge, collapsing regions 2 and 3 of the profile. This strong effect of the second moment can be understood by considering that low-variance phase functions (e.g., an uniform one) blur the internal reflection boundary (Figure 6) faster. As a result, the mid-order scattering component does not contribute to the local extrema, instead affecting the radiance profile in a way similar to high-order scattering. We discuss this effect in more detail in the supplementary material.

The above discussion suggests that we can compensate (approximately) for changes due to an increase in albedo by simultaneously increasing the phase function first moment. Similarly, we can increase the second moment to counter the effects of an increase in density. These relations are analogous to the *similarity relations* between scattering parameters that have been described and derived analytically for radiative transfer in the case of geometries where the radiance field is directionally bandlimited [26, 28]. These relations show that there exist material (approximate) scattering *material metamers* for the wedge geometry.

### 5.2. Refraction and Geometry Parameters

We now shift our attention to the refraction and geometry parameters of the wedge geometry describe in Section 2. We include here the refractive index, a material parameter, in this discussion, as refractive index affects the shape of the edge radiance profiles in a way much more similar to illumination and view angle than the other, scattering material parameters. Analogously to the previous subsection, throughout the discussion we make reference to Figure 9, which shows how the local radiance extrema change as a function of geometry and refraction parameters.

To produce the graphs in Figure 9, we have used only configurations of geometry and refractive index values where, with reference to Figure 4: 1) unscattered light rays reaching the right boundary of the wedge (point  $q_2$ ) are *totally* internally reflected; and 2) view rays left of the geometric edge ( $v_1$  and  $v_2$ ) intersect the internal reflection boundary. As we discuss in Section 3, the internally reflected lightfield and the fact that view rays integrate radiance from this lightfield are the reason why radiance profiles have local extrema features. When either of the above two assumptions is not satisfied, contributions from the internally reflected lightfield are very small to zero, resulting in the radiance extrema

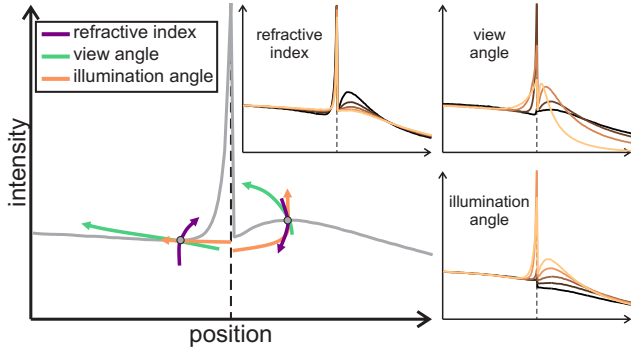


Figure 9: Effect of refraction and geometry parameters on the local extrema features of edge radiance profiles, as defined in Figure 3. The insets show representative sets of profiles where only the indicated parameter changes, with all other material and geometry parameters fixed.

being either very small or non-existent. The above assumptions are satisfied for the majority of geometric and refraction configurations we use in our database. For instance, condition 1 is satisfied for illumination angles  $\theta_i \geq 45^\circ$  when  $\eta = 1.3$ , and for all illumination angles when  $\eta \geq 1.4$ . Similar intervals can be derived easily for the view angles  $\theta_v$  that satisfy condition 2, for any given values of  $\eta$  and  $\theta_i$ . We discuss cases where either of these two assumptions is violated in the supplementary material.

Figure 9 indicates that it is impossible to create geometric metamers, unless we focus on only one side of the wedge. Changing one parameter to compensate for the effects of another parameter on the left side of the wedge, results on the opposite effect on the right side, and vice versa. We can intuitively explain this using the following geometric argument: A change in refractive index changes the directions at which illumination and view rays are refracted inside the medium. We can rotate the illumination direction so that the refracted direction, as well as the rest of their path inside the wedge, is exactly the same as previously. However, rotating the view direction only allows us to match the previous refracted direction of view rays on one side of the geometric edge and not both, because the angle of incidence of view rays left and right of the wedge. This geometric argument indicates that there are not “geometric metamers” for the entire radiance profile.

Finally, throughout this and the previous sections, we have assumed that the wedge angle  $\theta_w$  remains constant and equal to  $90^\circ$ . For smaller angles, there exists a range of illumination directions for which light rays reflect internally multiple times, alternating between the right and left boundaries. The presence of multiple reflection bounces complicates analysis considerably, so we will not discuss that case—though our discussion in the previous sections about the interaction between reflected light and scattering should

still provide some intuition about those cases. When the illumination direction does not result in multiple reflection bounces, our previous discussion continues to apply.

## 6. Implications for Computer Vision

We have presented a phenomenological study of the appearance of edges in images of translucent objects. Our study shows that translucent edges have specific qualitative features that arise as the result of the combination of scattering, refraction, and reflection. These features are robust to non-idealities of real-world objects, and distinguish translucent edges from edges in opaque objects. The features of a single edge profile contain information about all material parameters, density, albedo, phase function, and refractive index. This information, however, is confounded, in the sense that different materials can produce similar edge profile. Our analysis describes these classes of “material metamers”.

Our findings indicate that aggregating features from many different edges of a translucent object can provide rich information about the underlying material. This agrees with previous quantitative observations in material recognition [24], and motivates further research on the design of discriminative features based on the statistics of edge profiles. Additionally, the very different appearance of translucent and opaque edges implies that current edge detection and localization algorithms [22, 17], which are designed under an assumption of opacity, may be suboptimal for translucent objects. The characteristics of translucent edges might be used to design material-aware versions of such algorithms. Similarly, image denoising and deconvolution, and related applications such as depth-from-defocus and camera shake removal, often use priors based on the statistics of opaque edges [10, 25, 20, 19, 21, 5], and might benefit from new priors tailored for translucency. Finally, information from sharp geometric features of translucent objects can complement the information from smooth, near-flat regions used by current translucent photometric stereo and shape from “shading” algorithms [8, 15]. Our study shows that mid-order scattering is important for translucent edge appearance, implying that common approximations such as diffusion and single-scattering cannot be used to fully exploit edge profile information for the applications described above. Instead, data-driven, phenomenological approaches are more likely to be fruitful. Such approaches might benefit from the recent availability of large-scale material databases [3, 4].

**Acknowledgments:** We thank Bei Xiao and Shuang Zhao for helpful discussions. Funding provided by the NSF (IIS 1161564, 1012454, 1212928, 1011919), NIH (R01-EY019262-02, R21-EY019741-02) and AWS awards.

## References

- [1] Project page. <http://vision.seas.harvard.edu/translucentedges/>. 3
- [2] E. H. Adelson. On seeing stuff: the perception of materials by humans and machines. *Proceedings of the SPIE Vol. 4299, Human Vision and Electronic Imaging VI*, 2001. 1
- [3] S. Bell, P. Upchurch, N. Snavely, and K. Bala. Open-surfaces: A richly annotated catalog of surface appearance. *ACM Transactions on Graphics*, 2013. 8
- [4] S. Bell, P. Upchurch, N. Snavely, and K. Bala. Material recognition in the wild with the materials in context database. *IEEE CVPR*, 2015. 8
- [5] A. Chakrabarti and T. Zickler. Depth and deblurring from a spectrally-varying depth-of-field. *ECCV*, 2012. 8
- [6] S. Chandrasekhar. *Radiative transfer*. Dover, 1960. 2
- [7] T. Chen, H. Lensch, C. Fuchs, and H.-P. Seidel. Polarization and phase-shifting for 3d scanning of translucent objects. *IEEE CVPR*, 2007. 5
- [8] B. Dong, K. D. Moore, W. Zhang, and P. Peers. Scattering parameters and surface normals from homogeneous translucent materials using photometric stereo. *IEEE CVPR*, 2014. 8
- [9] C. Donner and H. Jensen. Rendering translucent materials using photon diffusion. *ACM SIGGRAPH 2008 Classes*, 2008. 4
- [10] R. Fergus, B. Singh, A. Hertzmann, S. T. Roweis, and W. T. Freeman. Removing camera shake from a single photograph. *ACM Transactions on Graphics*, 2006. 8
- [11] R. Fleming and H. Bülthoff. Low-level image cues in the perception of translucent materials. *ACM Transactions on Applied Perception*, 2005. 1
- [12] J. R. Frisvad, N. J. Christensen, and H. W. Jensen. Computing the scattering properties of participating media using lorenz-mie theory. 2007. 3
- [13] I. Gkioulekas, B. Xiao, S. Zhao, E. Adelson, T. Zickler, and K. Bala. Understanding the role of phase function in translucent appearance. *ACM Transactions on Graphics*, 2013. 1, 3, 7
- [14] I. Gkioulekas, S. Zhao, K. Bala, T. Zickler, and A. Levin. Inverse volume rendering with material dictionaries. *ACM Transactions on Graphics*, 2013. 3
- [15] C. Inoshita, Y. Mukaigawa, Y. Matsushita, and Y. Yagi. Surface normal deconvolution: Photometric stereo for optically thick translucent objects. *ECCV*, 2014. 8
- [16] A. Ishimaru. *Wave propagation and scattering in random media*. Wiley-IEEE, 1978. 2, 4
- [17] P. Isola, D. Zoran, D. Krishnan, and E. H. Adelson. Crisp boundary detection using pointwise mutual information. *ECCV*, 2014. 8
- [18] H. Jensen, S. Marschner, M. Levoy, and P. Hanrahan. A practical model for subsurface light transport. In *SIGGRAPH*, 2001. 4
- [19] N. Joshi, R. Szeliski, and D. Kriegman. Psf estimation using sharp edge prediction. *IEEE CVPR*, 2008. 8
- [20] A. Levin, R. Fergus, F. Durand, and W. T. Freeman. Image and depth from a conventional camera with a coded aperture. *ACM Transactions on Graphics*, 2007. 8
- [21] A. Levin, Y. Weiss, F. Durand, and W. Freeman. Understanding and evaluating blind deconvolution algorithms. *IEEE CVPR*, 2009. 8
- [22] D. R. Martin, C. C. Fowlkes, and J. Malik. Learning to detect natural image boundaries using local brightness, color, and texture cues. *IEEE PAMI*, 2004. 8
- [23] S. H. Mersch. *Polarized lighting for machine vision applications*. Society of Manufacturing Engineers, 1984. 5
- [24] L. Sharan, C. Liu, R. Rosenholtz, and E. Adelson. Recognizing materials using perceptually inspired features. *International Journal of Computer Vision*, 2013. 8
- [25] Y. Weiss and W. T. Freeman. What makes a good model of natural images? *CVPR*, 2007. 8
- [26] D. Wyman, M. Patterson, and B. Wilson. Similarity relations for the interaction parameters in radiation transport. *Applied optics*, 1989. 7
- [27] B. Xiao, B. Walter, I. Gkioulekas, T. Zickler, E. Adelson, and K. Bala. Looking against the light: how perception of translucency depends on lighting direction and phase function. *Journal of Vision*, 2014. 1, 7
- [28] S. Zhao, R. Ramamoorthi, and K. Bala. Higher-order similarity relations in radiative transfer. *ACM Transactions on Graphics*, 2014. 7